Applied Catalysis B: Environmental 325 (2023) 122342

Contents lists available at ScienceDirect

Applied Catalysis B: Environmental

journal homepage: www.elsevier.com/locate/apcatb

Insight into the strong Brönsted acid sites on isolated WO_x-modified Pt/zirconium phosphate for glycerol efficient hydrodeoxygenation

Huixiang Li [a], Yehong Wang [a,*], Chaofeng Zhang [b], Zhipeng Huang [a,c], Jianyu Han [a,c], Xuezhong Nie [a,c], Feng Wang [a,*]

[a] Dalian National Laboratory for Clean Energy, Dalian Institute of Chemical Physics, Chinese Academy of Sciences, 457 Zhongshan Road, Dalian 116023, Liaoning, China
[b] College of Light Industry and Food Engineering, Nanjing Forestry University, China
[c] University of Chinese Academy of Sciences, Beijing 100049, China

ARTICLE INFO

Keywords:
Glycerol
Brönsted acid
Hydrodeoxygenation
Zirconium phosphate
Tungsten oxide

ABSTRACT

Brönsted acidity of Pt/WO_x-based catalysts is crucial to efficient activation of C–OH bond in glycerol. Constructing strong Brönsted acidic sites (BAs) on catalysts is highly desired for efficient transformation of glycerol. Motivated by the source of Brönsted acidity in phosphotungstic acid, strong BAs were constructed on isolated WO_x-modified Pt/zirconium phosphate ($ZrPO_4$). Various characterizations confirm that the strong BAs on Pt-WO_x/$ZrPO_4$ are derived from the distinctive local structure of isolated W (V) oxides upon interacted with phosphate anion and zirconium center of $ZrPO_4$ through O–W–O groups. In addition, the strong Brönsted acidity of Pt-WO_x/$ZrPO_4$ contributes to the efficient C–OH activation and producing 46.2% of C3 hydrocarbons in yield in glycerol hydrodeoxygenation, which is superior to that over other reported Pt/WO_x catalysts. This work provides a strategy of fabricating strong BAs on solid catalysts and deep insight into the source of its Brönsted acidity for efficient transformation of C–OH in polyols.

1. Introduction

Polyol units widely exist in biomass-derived compounds, having the characteristic of abundant oxygen-containing groups in the structures. The transformation and utilization of polyols mainly involved deoxygenation processes, such as hydrodeoxygenation, and dehydration of the hydroxyl groups [1,2]. Glycerol represents one of the typical polyhydroxy compounds, obtained from renewable feedstocks (including vegetable oils, animal fats, lignocellulose, etc) via hydrolysis or hydrodeoxygenation, etc. Adding value to surplus glycerol has attracted significant attentions in recent decades through catalytic transformations [3–5]. Propanediol, propanol, or C3 hydrocarbons (propene, propane) can be obtained from glycerol through the deoxygenation process, which essentially involved the dissociation of secondary and primary C–OH bonds [6,7]. Thus C–OH activation becomes one of the significant determinants for the efficient utilization of aliphatic polyols.

The glycerol deoxygenation has been attempted using several types of catalysts: metal oxide modified noble catalysts (Pt-WO_x, Ir-ReO_x) [8,9], noble catalysts with an acid additive (Ru/C+Amberlyst 15, Ir-ReOx/SiO_2 + H_2SO_4) [10,11], and non-noble catalysts (Copper chromite, Cu-$H_4SiW_{12}O_{40}$/SiO_2, Cu-ZnO + H_2WO_4) [12,13]. The glycerol deoxygenation over the above catalysts is considered to be the C–OH dissociation over metal-acid bifunctional active sites through a mechanism of dehydration and hydrogenation, which is carried out with the synergestic catalysis of metal and acid sites [14–17]. Generally high dispersion of metal oxide or metal atoms corresponds to a large amount of Brönsted acid and metal sites, resulting in the high reaction activity [18]. Despite the numerous studies on various additives and supports to improve the Brönsted acidity and the dispersion of active sites on the surface of Pt/WO_x-based catalysts, the efficiency of C–OH transformation is still undesirable, always under high H_2 pressure (more than 4 MPa) or at expense of long reaction time (about 12 h or longer for obtaining a more than 70% conversion).[19–23] On the other hand, only propanediol and propanol are obtained from glycerol transformation in Pt/WO_x catalyzed reactions [24]. Although producing propene or propane (C3 hydrocarbon) from glycerol has been reported in other catalytic mixtures [25–28], such as Ru complex + HOTf and Ir-ReO_x/SiO_2 + HZSM-5, etc, Pt/WO_x-based catalysts have rarely achieved the

* Corresponding authors.
E-mail addresses: wangyehong@dicp.ac.cn (Y. Wang), wangfeng@dicp.ac.cn (F. Wang).

https://doi.org/10.1016/j.apcatb.2022.122342
Received 8 November 2022; Received in revised form 24 December 2022; Accepted 27 December 2022
Available online 28 December 2022

formation of C3 hydrocarbon. It seems that the activation of primary C–OH of propanol represents a more difficult barrier over Pt/WO_x-based catalysts. It is proposed that the Brönsted acidity generated on reported Pt/WO_x-based catalysts is insufficient to protonate the primary C–OH of propanol to give C3 hydrocarbons. Thus strong BAs on the surface of Pt/WO_x catalysts play a significant role in the efficient activation of C–OH in glycerol. However the creation of strong BAs on Pt/WO_x catalysts is challenging and the intrinsic structure of Brönsted acidic site is still elusive.

In this work, we aimed at creating strong BAs on Pt/WO_x-based catalysts for efficient hydrodeoxygenation of glycerol and providing insightful understanding for the intrinsic structure of strong BAs. Heteropolyacid represents one typical solid Brönsted acid, such as phosphotungstic acid, where the strong BAs are derived from the interaction between phosphate group and tungsten oxide. In addition, tungsten oxide loaded on ZrO_2 could promote the formation of strong BAs probably in the interfacial structure of WO_x and ZrO_2 [29–31]. Therefore, it is proposed that introducing phosphate group and zirconium cations into the Pt/WO_x-based solid catalysts probably induce the formation of strong BAs through interacting with WO_x. $ZrPO_4$ contains phosphate group and zirconium cations. Thus we fabricated WO_x-modified $ZrPO_4$ and further loaded Pt atoms on it, denoted as Pt-WO_x/$ZrPO_4$ catalyst for glycerol transformation. The strong Brönsted acidity of Pt-WO_x/$ZrPO_4$ was readily confirmed by infrared spectra of pyridine and ^{31}P NMR of TMPO adsorbed on the surface. We also explored the source of Brönsted acidity in Pt-WO_x/$ZrPO_4$ through careful characterizations. Overall, in this work we not only present a strategy of fabricating strong Brönsted acid sites on solid catalysts for efficient transformation of C–OH in glycerol, also provide deep understanding about the source of the strong Brönsted acidity of tungsten species.

2. Experimental procedures

2.1. Catalyst preparation

Zirconium phosphate ($ZrPO_4$) support was prepared by precipitation method using an appropriate solution of $NH_4H_2PO_4$ (1 M, 100 ml) and $ZrOCl_2$ (1 M, 50 ml). The slurry was stirred at RT for 4 h then washed with deionized water until the filtrate was neutral, followed by drying overnight at 100 °C to obtain $Zr(H_2PO_4)_2$ and calcination at 400 °C for 4 h in a tube furnace to obtain zirconium phosphate.

WO_x/$ZrPO_4$ was prepared by strong electrostatic adsorption wet impregnation technique combined with a simple filtration method using $ZrPO_4$ (3 g), and ammonium metatungstate (0.5 g). The mixture was stirred overnight at RT before filtration to remove excess solution, followed by drying at 100 °C for about 10 h, then calcinated at 500 °C for 4 h in a tube furnace. The amount of tungsten was calculated through inductively coupled plasma (ICP) analysis.

WO_x/Al_2O_3 was prepared through wetness impregnation according to the reported method [32]. The amount of tungsten was kept the same as that in WO_x/$ZrPO_4$.

Pt-WO_x/Support (Al_2O_3 and $ZrPO_4$), Pt/$ZrPO_4$ and Pt/WO_3 catalysts were prepared by incipient impregnation method using WO_x/Support, $ZrPO_4$ or WO_3 (3 g), solution of chloroplatinic acid (0.088 g/g, 1.8 g). The mixture was dried at 100 °C for about 12 h. Samples Pt-WO_x/Support, Pt/$ZrPO_4$ and Pt/WO_x can be obtained after reduction at 220 °C for 1 h under H_2.

2.2. Activity test

Catalytic testing was performed in a 30 ml stainless steel autoclave with an inserted Teflon vessel. An aqueous solution of glycerol (10 wt%) was placed into the autoclaves with a magneton and an appropriate amount of catalyst. After sealing the reactors, the air content was subsequently flushed 8 times with N_2 at 1 MPa. The reactor was then pressurized to target pressure with H_2 and heated under moderate agitation (500 rpm) to a final reaction temperature. The preheating time was set to be 20 min. After an appropriate reaction time, the reactors were cooled down and all the gases were collected in a gasbag. The autoclave contents were diluted to 10 times with CH_3CN upon adding internal standard 3-pentanol. The liquid products were analyzed using a gas chromatograph (Aglient Technoligies 7890B) equipped with a FID detector and a HP-Innowax capillary column. High performance liquid chromatography (HPLC) analysis for quantifying glycerol conversion was performed on an Agilent 1260 series with a refractive index detector and a PL Hi-Plex H column (300 × 7.7 mm, 8 μm). Diluted H_2SO_4 solution (5 mM) at a flow rate of 0.5 ml/min was used as the mobile phase. The column and detector temperatures were 65 °C and 50 °C, respectively. The gas products in the gasbag were analyzed using a gas chromatograph (Shimadzu; columns, CC 0.3 mm * 0.1 nm and PN 200 mm * 2.1 mm; TCD and FID detectors). The C3 hydrocarbon products were quantified by an internal standard method. Reusability test of catalyst was conducted under the same procedures above. After each reaction run, the catalyst was recovered, washed with distilled water and dried at 100 °C before the next reaction.

2.3. Catalyst characterization

Powder X-ray diffraction patterns (XRD) were obtained with a diffractometer from PANAlytical (X′pert Pro-1), using Cu-Kα radiation. Continuous scans were collected in the 2θ range of 20–80°, at a step rate of $10^{\circ}\cdot min^{-1}$.

Ultraviolet-visible (UV–vis) spectra were collected on a Shimadzu UV-2600 spectrophotometer. Inductively coupled plasma analysis for quantifying the loading of tungsten was performed on ICP-OES 7300DV (PerkinElmer).

An IR diffuse reflectance accessory was used for the Diffuse reflectance Fourier transform infrared spectroscopy (DRIFTS) measurements. The accessory was purchased from Pike Technologies. The MIR instrument model is Thermo Scientific Nicolet iS50 equipped with a mercury cadmium telluride (MCT) detector. The resolution is 4 cm^{-1} for the DRIFTS measurements using 64 scans. The sample was flushed with argon at room temperature for 1 h before the adsorption of probing gas CO.

Pyridine-adsorbed FTIR (Py-IR) spectra were recorded on a Brukers Optics XF808–04 instrument with a resolution better than 2 cm^{-1}. 15 mg catalyst was pressed into a self-supporting wafer of 13 mm in diameter and placed in an IR cell. Before the measurements, all the catalysts were pre-reduced under H_2 at 220 °C for 1 h and then cooled down to room temperature. Pyridine vapor was then introduced to the sample for adsorption and held for 30 min until saturation. After that, the spectra of pyridine chem-adsorbed on samples were collected upon the evacuation of physical-adsorbed and weakly chem-adsorbed pyridine at RT, 150 °C and 200 °C for 30 min, respectively.

NH_3-temperature programmed desorption (TPD) was conducted on a Micromeritics 2750 chemisorption apparatus equipped with a thermal conductivity detector (TCD). About 100 mg of the Pt-WO_x based catalysts was placed in a quartz tube and reduced at 493 K for 1 h in 10 vol% H_2/Ar flow (30 ml min^{-1}). WO_x/$ZrPO_4$ and $ZrPO_4$ were preheated at 500 °C for 30 min in He flow (30 ml min^{-1}). After being cooled down to 313 K, purge 5 vol% NH_3/He for 30 min. The catalyst was then purged by pure He for 60 min to remove the physical adsorbed NH_3. The desorption profile was acquired by heating the catalyst in He from 313 to 973 K at a ramping rate of 10 K min^{-1}.

H_2 pulse chemisorption was also conducted on a Micromeritics 2750 chemisorption apparatus equipped with a thermal conductivity detector (TCD). About 120 mg of the fresh and used Pt-WO_x/$ZrPO_4$ catalysts were placed in a quartz tube and reduced at 493 K for 1 h in 5 vol% H_2/Ar flow (30 ml min^{-1}). After being cooled down to 313 K, the catalyst was purged by pure Ar for 60 min (50 ml min^{-1}). Pulse-chemisorption of hydrogen was then performed at 313 K by injecting 5% H_2/Ar into a Ar

stream (50 ml min^{-1}) flowing over the reduced catalyst bed.

Solid-state ^{31}P NMR measurements were carried out on a 11.7 T wide-bore Bruker Avance III solid-state NMR spectrometer. A 4.0 mm Bruker multinuclear HX double resonance magic angle spinning (MAS) probe was used. The experiments were acquired at 25 °C and an MAS frequency of 10 kHz, controlled to within + /− 3 Hz using the Bruker MAS controller. It is noted that the Pt-WO_x based catalysts were pre-reduced at 220 °C in H_2 before the adsorption of TMPO. Samples for the ^{31}P NMR measurements were treated through the following procedures. First, a desirable amount of solid catalyst (about 0.3 g) was first placed in flask equipped with a vacuum stopcock. The flask containing the catalyst was then connected to a vacuum manifold for catalyst dehydration treatment at 150 °C under vacuum for 2.5 h. The flask containing the dehydrated catalyst was sealed and placed in glovebox filled with N_2. Then, a desirable amount (0.4 ml) of TMPO solution (170 mg/ml) in CH_2Cl_2, was syringed into the flask containing the dehydrated samples. The flask was then sealed, taken out from the glovebox and reconnected to the vacuum manifold, followed by removal of the CH_2Cl_2 solvent by evacuation at 50 °C for 15 min. Subsequently, the sample was subjected to a heating treatment at 170 °C for 1 h, prior to transferring to the glovebox again for NMR measurements.

The Raman spectra of samples were recorded at room temperature with a DL-UVRaman spectrometer (excitation line, 244 nm of an Ar^+ ion laser; source power, 30 ± 50 mW; resolution, 4 cm^{-1}, scanning time, 40 s for $ZrPO_4$; 100 s for $WO_x/ZrPO_4$ and Pt-$WO_x/ZrPO_4$).

The binding energy (B.E.) of catalysts was determined by X-ray photoelectron spectra (XPS) on an ESCALAB250 X-ray photoelectron spectrometer with surface carbon as the internal standard (C 1 s = 284.6 eV).

Sub-ångström resolution high-angle annular dark-field (HAADF) scanning transmission electron microscopy (STEM) images were obtained on a JEOL JEM-ARM200F STEM/transmission electron microscopy (TEM), also equipped with a CEOS probe corrector, at a resolution of 0.08 nm and energy dispersive X-ray spectroscopy (EDX). Before microscopy examination, the sample was dispersed onto a copper grid coated with a thin holey carbon film.

Zeta potential was measured with a laser nanosize analyser (Zetasizer Nano, Malvern). The sample was prepared by mixing $ZrPO_4$ (15 mg) and H_2O (8 ml), followed by static settlement overnight. Take the top liquid for the measurement of zeta potential.

3. Results and discussion

3.1. Synthesis strategy and acid properties of Pt-$WO_x/ZrPO_4$ catalyst

It is mentioned above that the fabrication of strong BAs can be probably realized by WO_x interacting with phosphate group and zirconium cation. Isolated dispersed WO_x or oligomers would probably promote enhancing the interaction with phosphate groups and zirconium cations. Meanwhile, zirconium phosphate is composed of phosphate groups and zirconium cations. Each of three oxygen atoms of the phosphate group is connected to a different zirconium, leading to a crosslinked network. The remaining P–OH group of the phosphate group leads to its Brönsted acidity and excellent cation-exchange capability [33,34]. The surface of $ZrPO_4$ is electronegative with a zeta potential of − 40.6 mV (Fig. S1a). In principle, H^+ on $ZrPO_4$ surface will be exchanged by the NH_4^+ cations of ammonium metatungstates in solution. The NH_4^+ or H^+ on the $ZrPO_4$ surface can coulombically attract tungsten anions, as shown in Fig. S1b. Thus strong electrostatic adsorption wet impregnation technique combined with a simple filtration method was used to promote attractive interactions between tungsten anions and NH_4^+ or H^+ on $ZrPO_4$ surface [35] and excess tungsten anions in solution were removed through filtration. It was expected that there was a high probability to produce isolated WO_x or oligomers on $ZrPO_4$. Pt ions were then uniformly loaded on WO_x modified $ZrPO_4$ through incipient-wetness impregnation to give the Pt-$WO_x/ZrPO_4$ catalyst upon reduction process (Fig. S2).

According to the designed synthesis approach above, two points need to be addressed urgently: the acidity properties of Pt-$WO_x/ZrPO_4$, the dispersion and local structure of WO_x. In the following, we provide solid evidences about the acidic properties of catalysts to demonstrate the hypothesis above through NH_3-TPD NMR and infrared spectroscopy.

First, NH_3-TPD technique was employed to probe the available surface acidity of the catalysts. Fig. 1a presents the NH_3-TPD profiles of Pt-WO_x based catalysts from 40 to 700 °C. The desorption peaks below 250 °C and in the region of 250–400 °C correspond to NH_3 desorption from weak acid sites and medium strong acid sites on the catalyst surface, respectively [36]. As displayed in Fig. 1a, Pt-$WO_x/ZrPO_4$ catalyst exhibited poorly resolved desorption peaks in two distinct temperature regions, centering at ca. 110 and 333 °C, which was ascribed to the weak and medium strong acidic sites on the surface and their amount was found to be 608.3 and 787.9 μmol/g, respectively. Then we compared its acidic properties with reference catalysts prepared by loading same amount of Pt-WO_x on Al_2O_3 to explore the role of $ZrPO_4$ in the acidic properties of Pt-$WO_x/ZrPO_4$. However, Pt-WO_x/Al_2O_3 exhibits only one obvious peak below 250 °C of NH_3 desorption from the weak acidic sites (475.3 μmol/g). Therefore Pt-$WO_x/ZrPO_4$ has larger amount and relatively stronger acidic sites on the surface than that on reference catalyst. $ZrPO_4$ plays essential roles in the formation of strong acidic sites on the surface of Pt-$WO_x/ZrPO_4$. We further studied the acidic properties of one and two components of Pt-$WO_x/ZrPO_4$ to identify the sources of its acidic sites as shown in Fig. 1b. All the catalysts present broad TPD profiles with two distinct desorption peaks in the temperature regions of below 250 °C and 250–400 °C, reflecting that the weak and medium strong acid sites are distributed on the surface. The amount of weak and medium strong acid sites on $ZrPO_4$ was found to be 370 and 402 μmol/g. It is noted that the addition of tungsten oxide on $ZrPO_4$ causes a decrease of the amount of NH_3 desorbed from weak and medium strong acid sites (308 and 245 μmol/g). Further, upon loading Pt on $WO_x/ZrPO_4$, large amount of weak and medium strong acid sites (608.3 and 787.9 μmol/g) were generated remarkably on the surface. Overall, Pt-$WO_x/ZrPO_4$ equips with more acidic sites on the surface in comparison with its one and two components. The extra generated acidic sites on Pt-$WO_x/ZrPO_4$ are probably associated with the reduction of Pt precursor in the catalyst preparation. The variation of acid amount caused by modifying WO_x or Pt on $ZrPO_4$ and the sources of the distinctive acid properties of Pt-$WO_x/ZrPO_4$ will be further explored by combining the NMR and infrared spectroscopy.

Probe molecules, pyridine and trimethylphosphine oxygen (TMPO) are expected to interact with two types of acidic sites, Brönsted acid sites and Lewis acid sites in distinct forms, which correspond to two characteristic spectroscopic signals of probe molecules on Brönsted and Lewis acid sites.[37,38] Specifically, the acid types of Pt-WO_x based catalysts were first identified by conducting the solid P NMR spectra of TMPO adsorbed on the surface of catalysts. Generally, TMPO bounds at Brönsted acid sites lead to ^{31}P resonance with $\delta^{31}P$ in a range of 40–80 ppm, while the signals responsible for TMPO attached on Lewis acid sites locate at around 37 ppm. In addition, the ^{31}P resonances of adsorbed TMPO with a larger $\delta^{31}P$ value represents a stronger acidity. As shown in Fig. 1c, there is a distribution of acid sites on the surface of Pt-WO_x based catalysts, Lewis acidic sites ($\delta^{31}P$, 39.4 ppm), weak Brönsted acid sites ($\delta^{31}P$, 40–60 ppm), and medium strong Brönsted acid sites ($\delta^{31}P > 60$ ppm) [38,39]. Obviously, strong Brönsted acid sites are prevailed on the surface of Pt-$WO_x/ZrPO_4$ due to the dominated ^{31}P resonances at 64.9 ppm in the range of 40–80 ppm, while reference catalyst Pt-WO_x/Al_2O_3 possess a large amount of weak Brönsted acid sites that retain TMPO molecules on the surface ($\delta^{31}P$, 55.8 and 49.6 ppm). Furthermore, we also analyzed the acidic properties of one and two components of Pt-$WO_x/ZrPO_4$ to identify the source of its acidity. Fig. 1d shows the ^{31}P NMR spectra of TMPO adsorbed on $ZrPO_4$, $WO_x/ZrPO_4$, Pt-$WO_x/ZrPO_4$. Apparently, both Lewis and Brönsted acid sites are distributed on their surface evidenced by the ^{31}P resonances of

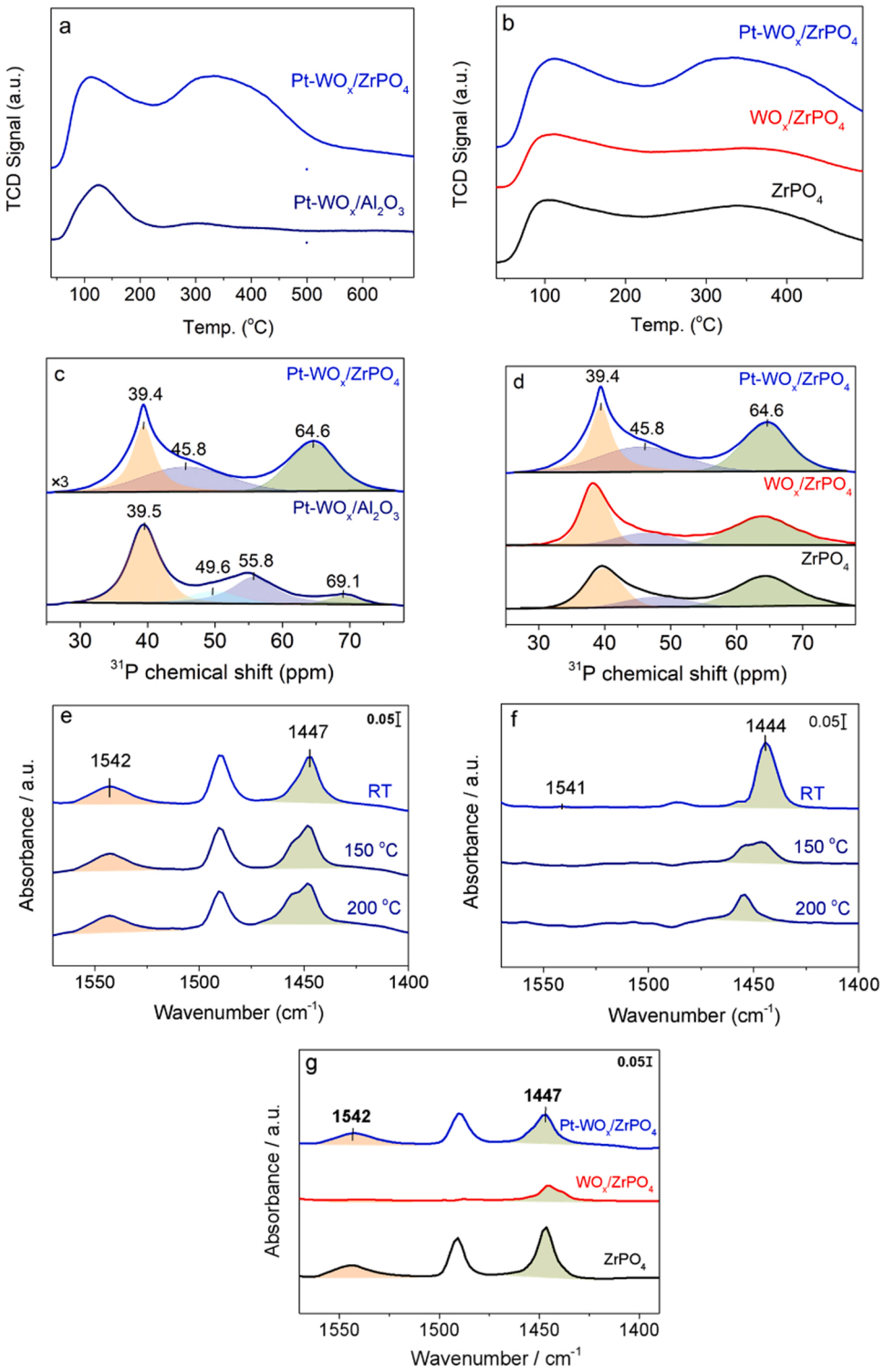

Fig. 1. Characterization of acidic properties of catalysts. NH_3-TPD profiles of Pt-WO_x based catalysts (a) and components of Pt-WO_x/$ZrPO_4$ (b); ^{31}P MAS NMR spectra of trimethylphosphine oxygen (TMPO) adsorbed on Pt-WO_x based catalysts (c) and components of Pt-WO_x/$ZrPO_4$ (d); Infrared spectra of pyridine adsorbed on Pt-WO_x/$ZrPO_4$ (e) Pt-WO_x/Al_2O_3 (f) recorded after evacuating weakly-adsorbed pyridine at RT, 150 °C and 200 °C for 30 min; Infrared spectra of pyridine adsorbed on components of Pt-WO_x/$ZrPO_4$ (g).

adsorbed TMPO with $\delta^{31}P$ at 39.4, 45.8 and 64.9 ppm. The relative amount of Brönsted acid sites distributed on each catalyst can be rough estimated according to the specific value of integration area of ^{31}P resonances of TMPO adsorbed on Brönsted acid sites and Lewis acid sites. The concentration ratio of Brönsted and Lewis acid site on $ZrPO_4$ corresponding to the ^{31}P resonances in the range of 40–80 and at 39.4 ppm were found to be 1.9 (Table S1). Upon loading WO_x on $ZrPO_4$, a decline of the concentration ratio was observed, down to 1.5. While the amount of Brönsted acid sites relative to Lewis acid sites increased again with a ratio of 2.1:1 after Pt was supported on WO_x/$ZrPO_4$.

Moreover, infrared spectra of pyridine absorption on catalysts were collected to explore the acid strength and amount of Pt-WO_x based catalysts, as shown in Fig. 1e-g. In general, the absorption band at 1542 cm^{-1} is associated with the vibrations of pyridine binding on Brönsted acid sites, and the band at around 1450 cm^{-1} corresponds to that on Lewis acid sites [21]. It is indicated that Lewis acid and Brönsted acid sites coexist on the surface of Pt-WO_x/$ZrPO_4$ according to the presence of absorption bands at 1542 cm^{-1} and 1447 cm^{-1} (Fig. 1e). Moreover the peak intensity of pyridine on Brönsted acid sites remained almost the same after evacuating at RT, 150 °C and 200 °C for 30 min

with Brönsted acid site concentration of about 67 μmol/g on the surface (Table S2), confirming the generation of medium strong Brönsted acid sites on Pt-$WO_x/ZrPO_4$. While, reference catalyst Pt-WO_x/Al_2O_3 exhibits a large amount of Lewis acidic sites (105.2 μmol/g) on the surface in the presence of dominated peak at around 1450 cm^{-1}. Meanwhile, the adsorption band of pyridine shift upwards by about 11 cm^{-1} gradually, which can be attributed to the removing of weakly adsorbed pyridine. Only a small amount of medium strong Lewis acidic sites (33.9 μmol/g) left on Pt-WO_x/Al_2O_3 upon elevating the evacuation temperature to 200 °C [40]. In addition, trace amount of strong BAs (1.3 μmol/g) was determined through the infrared spectra of pyridine adsorbed on reference catalyst Pt-WO_x/Al_2O_3 (Fig. 1f). Overall, it is indicated that Pt-$WO_x/ZrPO_4$ equips with larger amount of strong Brönsted acid sites on the surface than that on Pt-WO_x/Al_2O_3, which is consistent with the results of ^{31}P NMR of adsorbed TMPO. On the other hand, the acid properties of one and two components of Pt-$WO_x/ZrPO_4$ were also identified to study the acidity sources of Pt-$WO_x/ZrPO_4$. Fig. 1g showed the absorption spectra of pyridine on $WO_x/ZrPO_4$ and $ZrPO_4$. $ZrPO_4$ posses Lewis acid and Brönsted acid sites (118.7 and 70.8 μmol/g) on the surface due to the presence of the absorption bands of pyridine at 1542 cm^{-1} and 1447 cm^{-1} (Fig. 1g). However, after incorporating WO_x into $ZrPO_4$, most Brönsted acid sites disappeared evidenced by the weak absorption intensity of pyridine at 1542 cm^{-1} (5.4 μmol/g). According to the synthesis process of $WO_x/ZrPO_4$ mentioned above, the strong BAs, H^+ on $ZrPO_4$ surface can be exchanged by the NH_4^+ cations of ammonium metatungstates thus coulombically attract tungsten anions in solution. The disappearance of most Brönsted acidic sites on $WO_x/ZrPO_4$ can be contributed to the addition of ammonium metatungstates to replace part of H^+ sites in the liquid containing $ZrPO_4$ prior to high-temperature processing for loading WO_x on $ZrPO_4$. Upon loading Pt atoms on $WO_x/ZrPO_4$, the remarkable vibration band of pyridine on strong Brönsted acid sites (69.9 μmol/g) appeared again indicating the formation of a larger amount of Brönsted acid sites on the surface. Overall, both the ^{31}P NMR of adsorbed TMPO and infrared spectra of adsorbed pyridine indicated that a amount of Brönsted acid sites are formed in the process of supporting Pt on $WO_x/ZrPO_4$.

The additional generated strong BAs on Pt-$WO_x/ZrPO_4$ are proposed to relate to the reduction of Pt precursor in the catalyst preparation as illustrated above. As Pt^{4+} precursor is reduced to Pt by H_2, it is speculated that H_2 spillover can occur on Pt-WO_x based catalysts. H_2 molecule would dissociative chemisorb on Pt sites and the formed hydrogen atoms tend to spillover to the nearby WO_3 surface. These hydrogen atoms are very active and can induce the partial reduction of W═O in W^{6+} to W–OH in W^{5+} [15]. The formation of abundant reduced tungsten species on Pt-$WO_x/ZrPO_4$ was demonstrated by XPS results as illustrated in Fig. 2a. Broad bands in the range of 28–42 eV were composed of two doublets of W 4 f and Zr 4p component [41,42]. The dominated peaks at binding energies of 31.2 and 32.8 eV corresponded to $W4f_{7/2}$ and W 4 $f_{5/2}$ of W^{5+}, and another weak peaks at 36 and 37.6 eV were assigned to $W4f_{7/2}$ and $W4f_{5/2}$ of W^{6+} [41,42]. It is proposed that the W–OH in reduced W^{5+} oxides is probably contributed to the source of Brönsted acidity of Pt-$WO_x/ZrPO_4$ catalysts. However, W^{6+} was prevailed in Pt-WO_x/Al_2O_3 according to the W4f XPS results in Fig. 2b, where presents only two characteristic peaks of $W4f_{7/2}$ and $W4f_{5/2}$ of W^{6+}. Probably because that the reduced W^{5+} oxides remain unstable and can be readily re-transformed to W^{6+} oxides on the surface of Pt-WO_x/Al_2O_3. From the other aspect, it is indicated that the reduced tungsten oxides stay stable in Pt-$WO_x/ZrPO_4$ even during the ex-situ characterization. The distinctive properties of tungsten oxides in Pt-$WO_x/ZrPO_4$ probably associated with the local structure of tungsten oxide species, which will be explored in the following through spectroscopic characterizations.

3.2. Dispersion of Pt, WO_x and identification of tungsten species

Exploring the dispersion of each species and the structure of tungsten species appears crucial to understand the acid sources of Pt-$WO_x/ZrPO_4$. The bulk structural information was first analyzed by XRD, as shown in Fig. S3. The prefabricated $ZrPO_4$ material was regarded as an amorphous phase because of its poor crystallinity. The introduction of WO_x and Pt did not cause any obvious change in the original amorphous structure of $ZrPO_4$. There is no XRD patterns associated with Pt or WO_x species, preliminary indicating their high dispersion on the $ZrPO_4$ surface.

The dispersion of Pt atoms is further characterized by CO-adsorbed DRIFTS as shown in Fig. 3. The absorption of CO on Pt/$ZrPO_4$ and Pt-$WO_x/ZrPO_4$ shows a similar pattern. It produced one dominant band at 2082 cm^{-1}, corresponding to CO adsorbed on highly dispersed Pt sites with small particle size, and the other two weak bands at 2124 and 1862 cm^{-1}, assigned to CO on the positively charged Pt sites and relatively large Pt particles, respectively.[43] Overall, well-dispersed Pt atoms are prevailed on $ZrPO_4$ although the presence of relatively large Pt particles. Meanwhile, we also characterized the Pt dispersion on

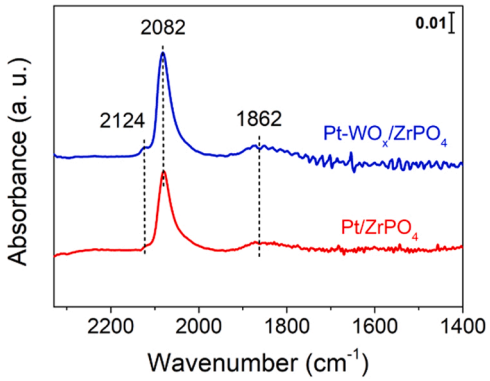

Fig. 3. Infrared spectra of CO adsorbed on Pt/$ZrPO_4$ and Pt-$WO_x/ZrPO_4$.

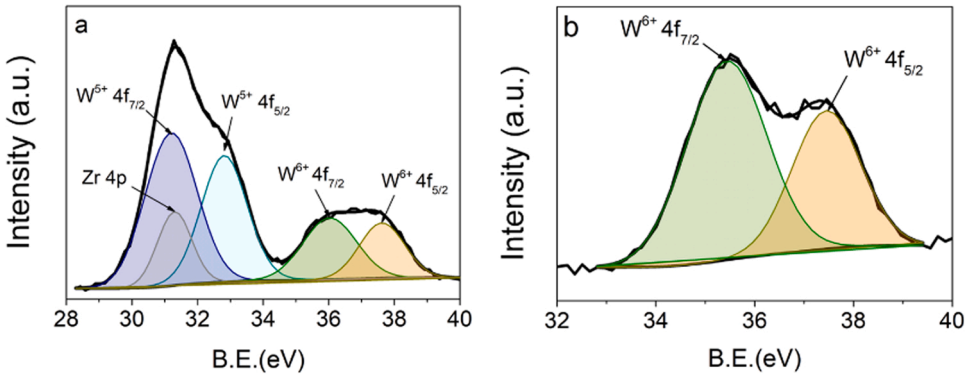

Fig. 2. W4f XPS photoemission peaks of (a) Pt-$WO_x/ZrPO_4$ and (b) Pt-WO_x/Al_2O_3 catalysts.

reference catalyst Pt-WO_x/Al_2O_3 with CO-adsorbed DRIFTS for comparison. It is indicated that Pt atoms also highly dispersed on reference catalyst, presenting major absorption bands of CO at 2082 cm^{-1} and 2124 cm^{-1} (Fig. S4, Supporting Information). Thus Pt atoms are highly dispersed on both Pt-$WO_x/ZrPO_4$ and Pt-WO_x/Al_2O_3 catalysts, which could provide rich sites for hydrogen activation.

Subsequently, HAADF-STEM was employed to further establish the high dispersion of Pt species and figure out the distribution of Pt and tungsten species on $ZrPO_4$. It was observed that Pt nanoparticles with an average of about 1.7 nm uniformly dispersed on Pt-$WO_x/ZrPO_4$. Less than 10% of Pt particles ranged from 3 to 5 nm in diameter. The lattice fringe of Pt (111) was also clearly presented in Fig. 4b. Additional images (Fig. S5, Supporting Information) from the examination of different regions all show the high dispersion of Pt particles with a small size on $ZrPO_4$. EDX mapping images (Fig. 4d, e) further confirm the formation of Pt nanoparticles and reveal that the tungsten species is well dispersed on $ZrPO_4$. Generally, Pt and WO_x species are dispersed separately on the surface of $ZrPO_4$. Moreover, the apparent dispersion of Pt on Pt-$WO_x/ZrPO_4$ surface has been estimated to be 13.8% by using pulse chemisorption of probe molecule H_2 (Fig. S6, Supporting Information).

In the following, UV–vis diffuse reflectance spectroscopy (DRS) is applied to investigate the local structure of tungsten species, according to the band positions of the ligand-to-metal charge transfer (LMCT) transitions of W(VI) oxide [29,44,45]. Fig. 5a shows the UV–vis absorption spectra of $ZrPO_4$, $WO_x/ZrPO_4$ and Pt-$WO_x/ZrPO_4$. The metal-free $WO_x/ZrPO_4$ sample displays one absorption band at 224 nm, which can be ascribed to the LMCT of isolated tetrahedral W(VI) oxide structures on the basis of detailed characterization of tungsten species in literature [29,44,45]. Upon loading Pt atoms on $WO_x/ZrPO_4$, the band of W(VI) oxide structures disappeared in the UV–vis spectrum, probably because the W(VI) species in Pt-$WO_x/ZrPO_4$ are reduced as illustrated by XPS results. For comparison, the UV–vis spectra of WO_x species loading on Al_2O_3 were also recorded, as shown in Fig. S7. The characteristic band of isolated tetrahedral W(VI) oxide species at around 228 nm is still present in the spectrum of Pt-WO_x/Al_2O_3. Therefore, it is demonstrated that W(VI) species still exist in Pt-WO_x/Al_2O_3, consistent with the W4f XPS results in Fig. 2b. In addition, we preliminarily speculate that the tungsten species are isolated dispersed on the supports, $ZrPO_4$ and Al_2O_3 from the absence of absorption band of polymeric tungsten (VI) oxide at 250–400 nm in Figs. 5a and S7.

Further, Raman spectroscopy was carried out to provide more information into the structural details of the tungsten species. W═O and W–O–W bonds are expected to exhibit characteristic Raman stretching modes in the region of 800–1000 cm^{-1} and 500–700 cm^{-1} respectively [30,45]. Fig. 5b displays the Raman spectra of $ZrPO_4$, $WO_x/ZrPO_4$ and Pt-$WO_x/ZrPO_4$ catalysts. $ZrPO_4$ presents several characteristic absorption bands at 1027, 604, 428, 279 cm^{-1}. Upon modifying $ZrPO_4$ with WO_x, one obvious broad Raman band of W═O appeared at around 845 cm^{-1}, indicating the presence of W═O in the local structure of W species in $WO_x/ZrPO_4$ [46,47]. While Pt-$WO_x/ZrPO_4$ presented a rather weak absorption band of W═O vibration in the inset spectra in Fig. 5. It is inferred only trace amount of W═O group existed in Pt-$WO_x/ZrPO_4$, which corresponds with the characterization results of UV–vis DRS and further demonstrates the reduced state of tungsten oxides is prevailed in Pt-$WO_x/ZrPO_4$. In addition, it is noted that Pt-$WO_x/ZrPO_4$ possesses additional bands at 334 cm^{-1}, associated with O–W–O bending mode of the surface WO_x species [45]. Thus the O–W–O groups are inferred to constitute the local structure of tungsten species in Pt-$WO_x/ZrPO_4$. Moreover, the characteristic bands of W–O–W vibration in the region of 500–700 cm^{-1} were not additionally generated both in the spectra of $WO_x/ZrPO_4$ and Pt-$WO_x/ZrPO_4$, further revealing the isolated dispersion of the tungsten oxide on $ZrPO_4$.

Overall, the combined Raman and UV–vis spectroscopic results, etc suggested that tungsten species are isolated dispersed on $ZrPO_4$. Most importantly, W–OH and O–W–O groups are probably present in the local structure of W (V) species in Pt-$WO_x/ZrPO_4$, which associate with the strong Brönsted acidity of Pt-$WO_x/ZrPO_4$. Therefore we propose that the local structure of tungsten oxide species is constituted by isolated W(V) oxide interacted with phosphate anion and zirconium center in $ZrPO_4$ through forming O–W–O bonds. In order to further demonstrated the specific local structure of tungsten oxide species, the evolution of chemical bonds on the surface during the catalyst preparation was tracked by FTIR. Fig. 6 shows the FTIR spectra of $ZrPO_4$, $WO_x/ZrPO_4$ and Pt-$WO_x/ZrPO_4$. $ZrPO_4$ presents characteristic bands of P–O–H deformation vibrations at about 2300 cm^{-1}, asymmetric stretching, and the bending vibration of –OH groups in the 1100–1700 cm^{-1} region. The

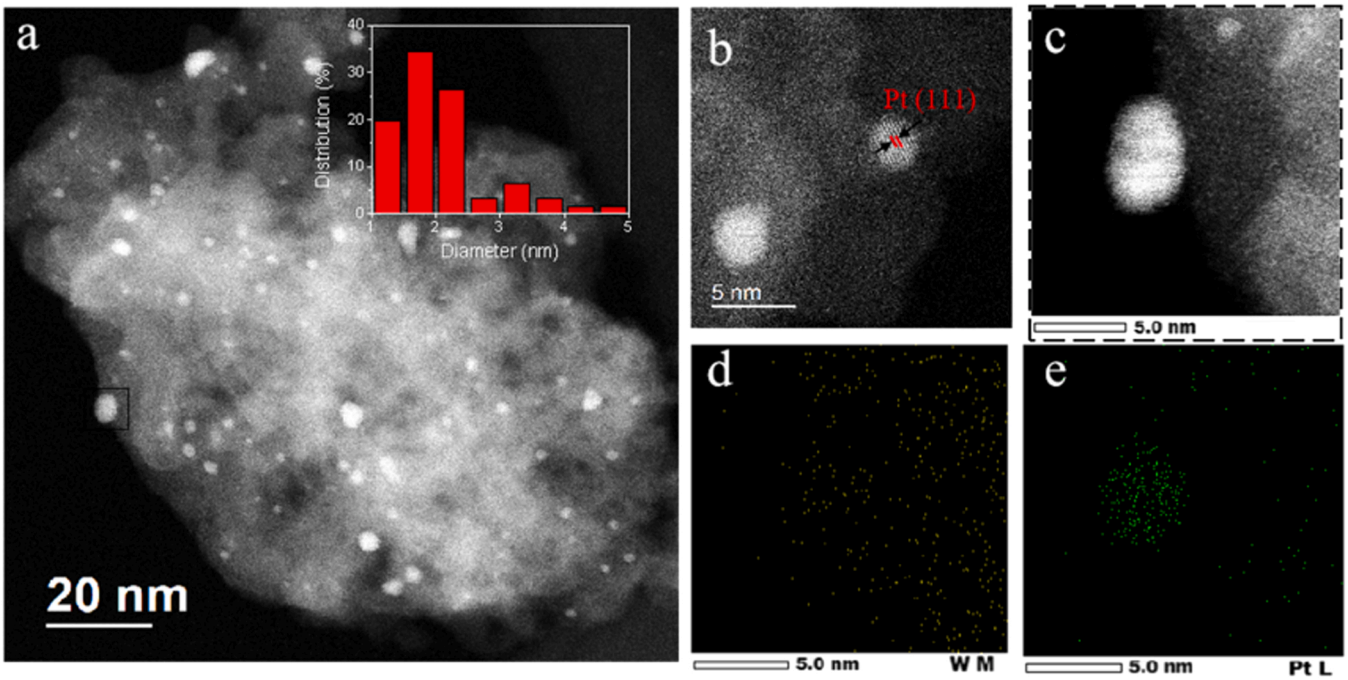

Fig. 4. HAADF-STEM images of Pt-$WO_x/ZrPO_4$ (a-c) and EDX mapping images of Pt-$WO_x/ZrPO_4$ (d, e).

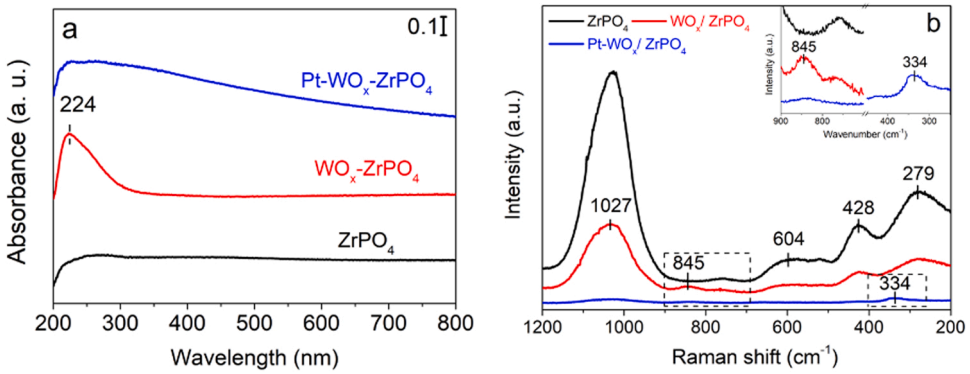

Fig. 5. (a) UV–vis DRS spectra (a) and Raman spectra (b) of $ZrPO_4$, $WO_x/ZrPO_4$ and Pt-$WO_x/ZrPO_4$ catalysts.

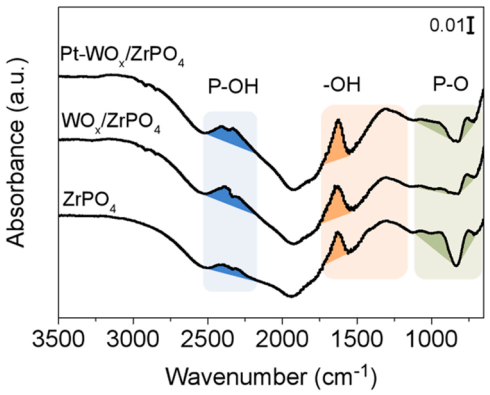

Fig. 6. FTIR spectra of $ZrPO_4$, $WO_x/ZrPO_4$, and Pt-$WO_x/ZrPO_4$.

transmission bands around 700–1100 cm^{-1} are assigned to the stretching and deforming vibration of skeleton P–O of $ZrPO_4$ [48].

Upon incorporating of WO_x to $ZrPO_4$, the absorption intensity of skeleton P–O became weaker; meanwhile, the intensity of OH bands increased, indicating the cleavage of P–O bonds and more OH groups formed on the surface. After Pt atoms were loaded on $WO_x/ZrPO_4$, there was an obvious increase in the absorption band of skeleton P–O at around 1000 cm^{-1} and surface –OH group in the 1100–1700 cm^{-1} region. It can be inferred the re-formation of skeleton P–O accompanied by the formation of OH group on the surface during the reduction process of Pt precursor under H_2. A rough model of the local structure of tungsten oxide in $WO_x/ZrPO_4$ and Pt-$WO_x/ZrPO_4$ was proposed in Scheme 1 on the basis of the above evolution of chemical bonds on the surface. The strong Brönsted acidity of Pt-$WO_x/ZrPO_4$ can be contributed to the W–OH species in the local structure of isolated W(V) oxide upon interacted with the phosphate anion and zirconium center through O–W–O bonds on the surface.

Therefore, the catalyst Pt-$WO_x/ZrPO_4$ has the following textural and acidic properties based on the characterization results mentioned above: (1) high dispersion of Pt atoms; (2) isolated W(V) oxide species; (3) distinctive local structure of WO_x upon interacted with phosphate anion and zirconium center on the surface; (4) strong Brönsted acidity. In comparison, although reference catalyst, Pt-WO_x/Al_2O_3 also equipped with high dispersion of Pt atoms and isolated tungsten oxide on the surface, the Brönsted acidity is negligible. The strong Brönsted acidity of Pt-$WO_x/ZrPO_4$, related with the local structure of isolated W(V) oxide upon interacted with the phosphate group and the zirconium cations in $ZrPO_4$, further demonstrated the previous hypothesis of creating strong BAs.

3.3. Catalytic performance and reaction mechanism

The deoxygenation activity of the prepared Pt-$WO_x/ZrPO_4$ was evaluated through glycerol transformation. The identification and quantification of products were performed with chromatography as described in the experimental section and the chromatograms were exhibited in Fig. S8. The catalytic performance of Pt-WO_x based catalysts was shown in Table 1. TOF values of Pt-WO_x based catalysts were estimated based on the highly dispersed tungsten oxides on the surface. Apparently, Pt-$WO_x/ZrPO_4$ gave the excellent catalytic activity compared with the reference catalyst Pt-WO_x/Al_2O_3 with a 79.6% of conversion and a markedly high TOF value at 200 $mol_{glycerol}\ mol_w^{-1}\ h^{-1}$ under same conditions (1 MPa H_2, 3 h, 200 °C). The initial reaction rate of Pt-$WO_x/ZrPO_4$ was estimated with a value of 0.65 $g_{glycerol}\ g_{cat}^{-1}\ h^{-1}$, over ten times of that of reference catalyst Pt-WO_x/Al_2O_3. Meanwhile, the reaction rate was also compared with other reported Pt-WO_x based catalysts in literature, further indicating the prominent activity of Pt-$WO_x/ZrPO_4$ for the transformation of C–OH under similar conditions (Table S3). The reaction process of glycerol transformation over Pt-$WO_x/ZrPO_4$ was proposed as the combination of glycerol hydrodeoxygenation to alcohols C3–OH, and the C3–OH dehydration followed by hydrogenation to propane (Scheme 2), where each step involves the protonation and activation of C–OH bond by BAs, i.e., the activity of glycerol transformation is closely related to the BAs of catalyst. Glycerol was totally converted by extending the reaction time to 5 h in Pt-$WO_x/ZrPO_4$ catalyzed reaction (Table 1). Meanwhile, nearly 50% of propane in yield was obtained by activating the three C–OH groups in glycerol, further demonstrating the high activity of Pt-$WO_x/ZrPO_4$ for transforming the C–OH.

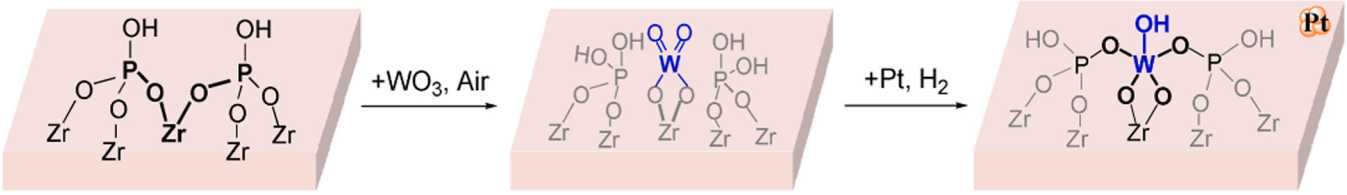

Scheme 1. Proposed local structure of W species in $WO_x/ZrPO_4$ and Pt-$WO_x/ZrPO_4$ on basis of the identification of tungsten species and the evolution of chemical bonds on the surface during the catalyst preparation.

Table 1
Catalytic performance of glycerol hydrodeoxygenation over Pt-WO_x based catalysts.

Catalyst	Conv. %	Time / h	Yield %			Initial reaction rate ($g_{glycerol}$ g_{cat}^{-1} h^{-1})	TOF[&] ($mol_{glycerol}$ mol_{w}^{-1} h^{-1})
			1, 3-PD[$]	1-Propanol	Propane		
Pt-WO_x/Al_2O_3	9.9	3	2.7	2.5	4.7	0.05	25.17
Pt-WO_x/$ZrPO_4$	16.4	0.38 *	1.4	11.7[#]	2.3	0.65	326.49
	79.6	3	12.6	34.3	27.6	–	200.37
	99.7	5	8.0	45.8	46.2	–	150.54

Reaction conditions: catalyst 0.2 g, 10 wt% glycerol 3 g, 200 °C, 1 MPa H_2, 3 h; *including the preheating time 20 min; [&] the number of glycerol converted per hour per tungsten oxide. [$] 1, 3-propanediol. [#] 1-propanol, 4.4%; 2-propanol, 7.3%.

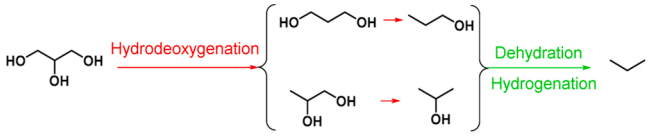

Scheme 2. Reaction flow of glycerol deoxygenation to C3 chemicals.

In order to identify the reaction active sites, the performance of each species in Pt-WO_x/$ZrPO_4$ for glycerol transformation was evaluated as shown in Fig. 7. Obviously, only Pt-WO_x/$ZrPO_4$ presents excellent performance; $ZrPO_4$ or any combination of two species has little glycerol conversion. In addition, the same trend was also observed in the deoxygenation reactions of propanediol and propanol (Fig. S9). Pt-WO_x/$ZrPO_4$ gave the most C3 hydrocarbon products in C3–OH transformations. It can be inferred the synergistic effect of three active species in Pt-WO_x/$ZrPO_4$ for efficient C–OH transformation to C3 chemicals.

Moreover, we focused on identifying the active sites and their synergistic effect, which contribute to the prominent performance of Pt-WO_x/$ZrPO_4$ through combining the characterization results above about the acid properties and dispersion of metal and metal oxide. On one hand, high dispersion of Pt and WO_x on $ZrPO_4$ could certainly provide rich active sites and promote the transformation of glycerol. Reference catalyst Pt-WO_x/Al_2O_3 and the reported catalysts also have high density of Pt and WO_x sites but show poor catalytic activity. Thus, the outstanding catalytic performance of Pt-WO_x/$ZrPO_4$ for glycerol deoxygenation cannot be solely attributed to the high dispersion of active sites. On the other hand, strong Brönsted acid sites on the catalyst surface play crucial role on the activation of C–OH in glycerol. Although $ZrPO_4$ and Pt/$ZrPO_4$ also have strong Brönsted acid sites characterized above by the infrared spectra of adsorbed pyridine in Figs. 1 and S10, their performance for propanol and propanediol transformation is unsatisfactory compared with that of Pt-WO_x/$ZrPO_4$ (Fig. S9). Thus the intrinsic acidity of $ZrPO_4$ did not dominate the activation of C–OH. Besides, most intrinsic Brönsted acid sites on $ZrPO_4$ were consumed after decorating WO_x as illustrated by the infrared spectra of adsorbed pyridine in Fig. 1. The strong Brönsted acidity of Pt-WO_x/$ZrPO_4$ associated with the distinctive local structure of isolated WO_x upon interacted with $ZrPO_4$ (Scheme 1), therefore contributes to its highly efficient deoxygenation reaction of glycerol through the efficient protonation and activation of C–OH by strong Brönsted acidic sites.

Fig. 7 also shows the catalytic performance of Pt-WO_x/$ZrPO_4$ and physical mixtures of Pt/$ZrPO_4$ and WO_x/$ZrPO_4$. Pt-WO_x/$ZrPO_4$ represents the ideal catalyst; moderate amount of deoxygenation products was still achieved in the reactions catalyzed by the physical mixtures of Pt and WO_x species. This experimental results revealed the existence of hydrogen spillover on $ZrPO_4$. The catalytic process over Pt-WO_x/$ZrPO_4$ through the synergistic catalysis of three species, Pt, WO_x and $ZrPO_4$ is proposed as following: Pt served as activating H_2; activated hydrogen was migrated to WO_x on $ZrPO_4$; WO_x was subsequently reduced by the spillover hydrogen to generate strong Brönsted acid sites, which contributed to the efficient protonation and transformation of C–OH groups in glycerol (Fig. 8). In addition, the performance of Pt-WO_x/$ZrPO_4$ for 1-propanol dehydration dropped dramatically after the reaction atmosphere was transferred to inert argon as shown in Fig. S9. It further confirmed that the strong Brönsted acid sites can be generated under H_2 and contribute to the activation of C–OH. However, despite Pt-WO_x/$ZrPO_4$ equips with highly efficient performance of C–O bond transformation, the reusability test indicated the catalytic activity declined notably after three successive runs (Fig. S11), Further, we conducted H_2 pulse chemisorption to analyze the apparent dispersion of Pt on the surface of used catalyst. (Fig. S6) It was demonstrated that Pt aggregated after the reaction with a decreased Pt dispersion to 8%, probably contributed to the declined reaction activity. Developing highly stable Pt/WO_x based catalyst is the next goal for the efficient conversion of glycerol [49].

4. Conclusion

This work focused on studying the strong Brönsted acid sites on Pt/WO_x-based catalyst for efficient transformation of polyol groups in biomass-derived compounds. Isolated WO_x-modified Pt/$ZrPO_4$ was rationally fabricated through strong electrostatic adsorption wet impregnation technique. It is revealed that the Brönsted acidity of the as-prepared Pt-WO_x/$ZrPO_4$ significantly overwhelms that of reference

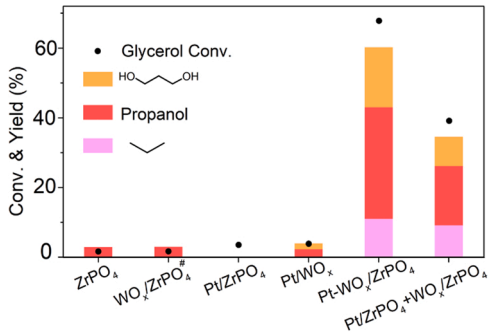

Fig. 7. Glycerol hydrodeoxygenation over various catalysts, Pt-WO_x/$ZrPO_4$ and physical mixtures of Pt/$ZrPO_4$ and WO_x/$ZrPO_4$. 165 °C, 6 h, 1 MPa H_2, catalyst 0.2 g, 10 wt% glycerol 3 g, [#]2 MPa H_2.

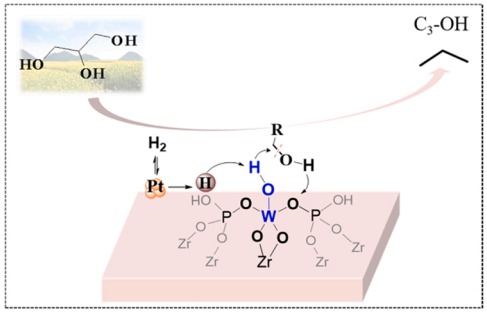

Fig. 8. Proposed catalytic mechanism of glycerol hydrodeoxygenation to C3 chemicals over Pt and strong Brönsted acid sites concerted Pt-WO_x/$ZrPO_4$ catalyst.

catalyst, Pt-WO_x/Al_2O_3, in terms of acid concentration and strength. Moreover, spectroscopic characterization results further demonstrated that the strong BAs on Pt-$WO_x/ZrPO_4$ are probably derived from the distinctive local structures of W(V) oxide species, formed by interacting with phosphate group and zirconium anion through O–W–O bonds. The catalytic performance of Pt-$WO_x/ZrPO_4$ was evaluated in glycerol hydrodeoxygenation. It presents excellent catalytic activity (79.6% of conversion at 200 °C, 1 MPa H_2 for 3 h), nearly eight times that of Pt-WO_x/Al_2O_3. Remarkably, a considerable amount of C3 hydrocarbon product (nearly 50% yield) can also be formed from glycerol over Pt-$WO_x/ZrPO_4$. Overall, this work presents a strategy of fabricating strong BAs on solid catalyst for the efficient transformation of polyols, glycerol and provides vital insight into the source of strong BAs, contributing to the highly efficient utilization of biomass resources.

CRediT authorship contribution statement

Huixiang Li: Conceptualization, Methodology, Investigation, Formal analysis, Writing – original draft, Writing – review & editing. **Yehong Wang**: Conceptualization, Methodology, Writing – original draft, Writing – review & editing, Funding acquisition, Project administration. **Chaofeng Zhang**: Investigation, Formal analysis, Writing – original draft, Writing – review & editing. **Zhipeng Huang**: Investigation, Formal analysis, Writing – original draft, Writing – review & editing. **Jianyu Han**: Investigation, Formal analysis, Writing – review & editing. **Xuezhong Nie**: Investigation, Formal analysis. **Feng Wang**: Conceptualization, Methodology, Writing – original draft, Writing – review & editing, Funding acquisition, Project administration.

Declaration of Competing Interest

The authors declare that they have no known competing financial interests or personal relationships that could have appeared to influence the work reported in this paper.

Data availability

Data will be made available on request.

Acknowledgments

This work was supported by the National Natural Science Foundation of China (22025206, 22202196 , 21972139, 21721004, 21991090), the Fundamental Research Funds for the Central Universities (20720220008) and the Youth Innovation Promotion Association (YIPA) of the Chinese Academy of Sciences (2019185).

Appendix A. Supporting information

Supplementary data associated with this article can be found in the online version at doi:10.1016/j.apcatb.2022.122342.

References

[1] A.M. Ruppert, K. Weinberg, R. Palkovits, Hydrogenolysis goes bio: from carbohydrates and sugar alcohols to platform chemicals, Angew. Chem. Int. Ed. 51 (2012) 2564–2601, https://doi.org/10.1002/anie.201105125.
[2] R. Wei, X. Qu, Y. Xiao, J. Fan, G. Geng, L. Gao, G. Xiao, Hydrogenolysis of glycerol to propanediols over silicotungstic acid catalysts intercalated with CuZnFe hydrotalcite-like compounds, Catal. Today 368 (2021) 224–231, https://doi.org/10.1016/j.cattod.2020.11.028.
[3] A. Brandner, K. Lehnert, A. Bienholz, M. Lucas, P. Claus, Production of biomass-derived chemicals and energy: chemocatalytic conversions of glycerol, Top. Catal. 52 (2009) 278–287, https://doi.org/10.1007/s11244-008-9164-2.
[4] A. Behr, J. Eilting, K. Irawadi, J. Leschinski, F. Lindner, Improved utilisation of renewable resources: New important derivatives of glycerol, Green. Chem. 10 (2008) 13–30, https://doi.org/10.1039/b710561d.
[5] U.I. Nda-Umar, I. Ramli, Y.H. Taufiq-Yap, E.N. Muhamad, An overview of recent research in the conversion of glycerol into biofuels, fuel additives and other bio-based chemicals, Catalysts 9 (2019) 15–61, https://doi.org/10.3390/catal9010015.
[6] Y. Wang, J. Zhou, X. Guo, Catalytic hydrogenolysis of glycerol to propanediols: a review, RSC Adv. 5 (2015) 74611–74628, https://doi.org/10.1039/C5RA11957J.
[7] D. Sun, Y. Yamada, S. Sato, W. Ueda, Glycerol hydrogenolysis into useful C3 chemicals, Appl. Catal. B: Environ. 193 (2016) 75–92, https://doi.org/10.1016/j.apcatb.2016.04.013.
[8] F. Wu, H. Jiang, X. Zhu, R. Lu, L. Shi, F. Lu, Effect of Tungsten Species on Selective Hydrogenolysis of Glycerol to 1,3-Propanediol, ChemSusChem 14 (2021) 569–581, https://doi.org/10.1002/cssc.202002405.
[9] Y. Nakagawa, K. Tomishige, Heterogeneous catalysis of the glycerol hydrogenolysis, Catal. Sci. Technol. 1 (2011) 179–190, https://doi.org/10.1039/c0cy00054j.
[10] T. Miyazawa, S. Koso, K. Kunimori, K. Tomishige, Development of a Ru/C catalyst for glycerol hydrogenolysis in combination with an ion-exchange resin, Appl. Catal. A-Gen. 318 (2007) 244–251, https://doi.org/10.1016/j.apcata.2006.11.006.
[11] Y. Nakagawaa, Y. Shinmi, S. Koso, K. Tomishige, Direct hydrogenolysis of glycerol into 1,3-propanediol over rhenium-modified iridium catalyst, J. Catal. 272 (2010) 191–194, https://doi.org/10.1016/j.jcat.2010.04.009.
[12] J. Chaminand, La Djakovitch, P. Gallezot, P. Marion, C. Pinel, C. Rosier, Glycerol hydrogenolysis on heterogeneous catalysts, Green. Chem. 6 (2004) 359–361, https://doi.org/10.1039/b407378a.
[13] L. Huang, Y. Zhu, H. Zheng, G. Ding, Y. Li, Direct Conversion of Glycerol into 1,3-Propanediol over Cu-H4SiW12O40/SiO2 in Vapor Phase, Catal. Lett. 131 (2009) 312–320, https://doi.org/10.1007/s10562-009-9914-1.
[14] N. Lei, A. Wang, X. Zhao, B. Hou, M. Yang, M. Zhou, F. Liu, A. Wang, T. Zhang, Effective Hydrogenolysis of Glycerol to 1,3-Propanediol over Metal-Acid Concerted Pt/WOx/Al_2O_3 Catalysts, ChemCatChem 11 (2019) 1–11, https://doi.org/10.1002/cctc.201900689.
[15] W. Zhou, Y. Li, X. Wang, D. Yao, Y. Wang, S. Huang, W. Li, Y. Zhao, S. Wang, X. Ma, Insight into the nature of Brönsted acidity of Pt-$(WO_x)_n$-H model catalysts in glycerol hydrogenolysis, J. Catal. 388 (2020) 154–163, https://doi.org/10.1016/j.jcat.2020.05.019.
[16] B. Zhao, Y. Liang, L. Liu, Q. He, J.-X. Dong, Facilitating Pt-WOx species interaction for efficient glycerol hydrogenolysis to 1,3-propanediol, ChemCatChem 13 (2021) 3695–3705, https://doi.org/10.1002/cctc.202100773.
[17] W. Zhou, Y. Zhao, Y. Wang, S. Wang, X. Ma, Glycerol Hydrogenolysis to 1,3-Propanediol on Pt/WO_3/ZrO_2: Hydrogen Spillover Facilitated by Pt(111) Formation, ChemCatChem 8 (2016) 3663–3671, https://doi.org/10.1002/cctc.201600981.
[18] B. Zhao, Y. Liang, W. Yan, L. Liu, J. Dong, A Facile Approach to Tune WO_x Species Combining Pt Catalyst for Enhanced Catalytic Performance in Glycerol Hydrogenolysis, Ind. Eng. Chem. Res. 60 (2021) 12534–12544, https://doi.org/10.1021/acs.iecr.1c02184.
[19] J. Oh, S. Dash, H. Lee, Selective conversion of glycerol to 1,3-propanediol using Pt-sulfated zirconia, Green. Chem. 12 (2011) 2004–2007, https://doi.org/10.1039/c1gc15263g.
[20] X. Zhang, G. Cui, H. Feng, L. Chen, H. Wang, B. Wang, X. Zhang, L. Zheng, S. Hong, M. Wei, Platinum–copper single atom alloy catalysts with high performance towards glycerol hydrogenolysis, Nat. Commun. 10 (2019) 5812–5823, https://doi.org/10.1038/s41467-019-13685-2.
[21] Y. Fan, S. Cheng, H. Wang, J. Tian, S. Xie, Y. Pei, M. Qiao, B. Zong, Pt–WO_x on monoclinic or tetrahedral ZrO_2: Crystal phase effect of zirconia on glycerol hydrogenolysis to 1,3-propanediol, Appl. Catal. B: Environ. 217 (2017) 331–341, https://doi.org/10.1016/j.apcatb.2017.06.011.
[22] Y. Fan, S. Cheng, Hao Wang, D. Ye, S. Xie, Y. Pei, H. Hu, W. Hua, Z.H. Li, M. Qiao, B. Zong, Nanoparticulate Pt on mesoporous SBA-15 doped with extremely low amount of W as a highly selective catalyst for glycerol hydrogenolysis to 1,3-propanediol, Green. Chem. 19 (2017) 2174–2183, https://doi.org/10.1039/c7gc00317j.
[23] L. Gong, Y. Lu, Y. Ding, R. Lin, J. Li, W. Dong, T. Wang, W. Chen, Selective hydrogenolysis of glycerol to 1,3-propanediol over a Pt/$WO_3/TiO_2/SiO_2$ catalyst in aqueous media, Appl. Catal. A-Gen. 390 (2010) 119–126, https://doi.org/10.1016/j.apcata.2010.10.002.
[24] J. Wang, M. Yang, A. Wang, Selective hydrogenolysis of glycerol to 1,3-propanediol over Pt-W based catalysts, Chin. J. Catal. 41 (2020) 1311–1319, https://doi.org/10.1016/S1872-2067(20)63586-0.
[25] Y. Nakagawa, M. Tamura, K. Tomishige, Perspective on catalyst development for glycerol reduction to C3 chemicals with molecular hydrogen, Res. Chem. Intermed. 44 (2018) 3879–3903, https://doi.org/10.1007/s11164-018-3481-2.
[26] Z.Y. Zakaria, N.A.S. Amin, J. Linnekoski, A perspective on catalytic conversion of glycerol to olefins, Biomass-.-. Bioenergy 55 (2013) 370–385, https://doi.org/10.1016/j.biombioe.2013.02.014.
[27] K. Chen, M. Tamura, Z. Yuan, Y. Nakagawa, K. Tomishige, One-pot conversion of sugar and sugar polyols to n-alkanes without C-C Dissociation over the Ir-ReO_x/SiO_2 catalyst combined with H-ZSM-5, ChemSusChem 6 (2013) 613–621, https://doi.org/10.1002/cssc.201200940.
[28] D. Taher, M.E. Thibault, D. Di Mondo, M. Jennings, M. Schlaf, Acid-, water- and high-temperature-stable ruthenium complexes for the total catalytic deoxygenation of glycerol to propane, Chemistry 15 (2009) 10132–10143, https://doi.org/10.1002/chem.200901427.
[29] A. Guntida, K. Suriye, J. Panpranot, P. Praserthdam, Lewis acid transformation to Bronsted acid sites over supported tungsten oxide catalysts containing different surface WO_x structures, Catal. Today 358 (2020) 354–369, https://doi.org/10.1016/j.cattod.2019.07.019.

[30] K. Song, H. Zhang, Y. Zhang, Y. Tang, K. Tang, Preparation and characterization of WO_x/ZrO_2 nanosized catalysts with high WO_x dispersion threshold and acidity, J. Catal. 299 (2013) 119–128, https://doi.org/10.1016/j.jcat.2012.11.011.
[31] T. Onfroy, G. Clet, M. Houalla, Development of acidic sites in WO_x/ZrO_2, Chem. Comm. (2001) 1378–1379, https://doi.org/10.1039/b102867g.
[32] B. Wang, F. Liu, W. Guan, A. Wang, T. Zhang, Promoting the Effect of Au on the Selective Hydrogenolysis of Glycerol to 1,3-Propanediol over the $Pt/WO_x/Al_2O_3$ Catalyst, ACS Sustain. Chem. Eng. 9 (2021) 5705–5715, https://doi.org/10.1021/acssuschemeng.1c00880.
[33] H. Xiao, S. Liu, Zirconium phosphate (ZrP)-based functional materials: Synthesis, properties and applications, Mater. Des. 155 (2018) 19–35, https://doi.org/10.1016/j.matdes.2018.05.041.
[34] B. Pan, Q. Zhang, W. Du, W. Zhang, B. Pan, Q. Zhang, Z. Xu, Q. Zhang, Selective heavy metals removal from waters by amorphous zirconium phosphate: behavior and mechanism, Water Res 41 (2007) 3103–3111, https://doi.org/10.1016/j.watres.2007.03.004.
[35] L. DeRita, S. Dai, K. Lopez-Zepeda, N. Pham, G.W. Graham, X. Pan, P. Christopher, Catalyst Architecture for Stable Single Atom Dispersion Enables Site-Specific Spectroscopic and Reactivity Measurements of CO Adsorbed to Pt Atoms, Oxidized Pt Clusters, and Metallic Pt Clusters on TiO_2, J. Am. Chem. Soc. 139 (2017) 14150–14165, https://doi.org/10.1021/jacs.7b07093.
[36] S. Zhu, X. Gao, Y. Zhu, Y. Li, Promoting effect of WO_x on selective hydrogenolysis of glycerol to 1,3-propanediol over bifunctional $Pt–WO_x/Al_2O_3$ catalysts, J. Mol. Catal. A-Chem. 398 (2015) 391–398, https://doi.org/10.1016/j.molcata.2014.12.021.
[37] Y. Wang, J. Liu, Z. Zhao, Q. Guo, Q. Jiang, N. He, F. Wang, A carbon-negative route for sustainable production of aromatics from biomass-derived aqueous oxygenates, Appl. Catal. B: Environ. 307 (2022) 121139–121148, https://doi.org/10.1016/j.apcatb.2022.121139.
[38] A. Zheng, S.B. Liu, F. Deng, 31P NMR chemical shifts of phosphorus probes as reliable and practical acidity scales for solid and liquid catalysts, Chem. Rev. 117 (2017) 12475–12531, https://doi.org/10.1021/acs.chemrev.7b00289.
[39] A. Zheng, S. Li, S.B. Liu, F. Deng, Acidic properties and structure-activity correlations of solid acid catalysts revealed by solid-state NMR spectroscopy, Acc. Chem. Res 49 (2016) 655–663, https://doi.org/10.1021/acs.accounts.6b00007.
[40] G. Busca, The surface acidity of solid oxides and its characterization by IR spectroscopic methods. An attempt at systematization, Phys. Chem. Chem. Phys. 1 (1999) 723–736, https://doi.org/10.1039/A808366E.
[41] M. Sun, S. Wang, Y. Li, H. Xu, Y. Chen, Promotion of catalytic performance by adding W into Pt/ZrO_2 catalyst for selective catalytic oxidation of ammonia, Appl. Surf. Sci. 402 (2017) 323–329, https://doi.org/10.1016/j.apsusc.2016.12.241.
[42] S. Zhu, X. Gao, Y. Zhu, J. Cui, H. Zheng, Y. Li, SiO2 promoted $Pt/WO_x/ZrO_2$ catalysts for the selective hydrogenolysis of glycerol to 1,3-propanediol, Appl. Catal. B: Environ. 158–159 (2014) 391–399, https://doi.org/10.1016/j.apcatb.2014.04.049.
[43] B. Zhao, Y. Liang, L. Liu, Q. He, J. Dong, Discovering positively charged Pt for enhanced hydrogenolysis of glycerol to 1,3-propanediol, Green. Chem. 22 (2020) 8254–8259, https://doi.org/10.1039/d0gc03364b.
[44] J.-C. Hu, Y.-D. Wang, L.-F. Chen, R. Richards, W.-M. Yang, Z.-C. Liu, W. Xu, Synthesis and characterization of tungsten-substituted SBA-15: An enhanced catalyst for 1-butene metathesis, Microporous Mesoporous Mater. 93 (2006) 158–163, https://doi.org/10.1016/j.micromeso.2006.02.019.
[45] E.I. Ross-Medgaarden, I.E. Wachs, Structural Determination of Bulk and Surface Tungsten Oxides with UV–vis Diffuse Reflectance Spectroscopy and Raman Spectroscopy, J. Phys. Chem. C. 111 (2007) 15089–15099, https://doi.org/10.1021/jp074219c.
[46] S. Bhowmik, N. Enjamuri, S. Darbha, Hydrogenolysis of glycerol in an aqueous medium over Pt/WO_3/zirconium phosphate catalysts studied by 1H NMR spectroscopy, N. J. Chem. 45 (2021) 5013–5022, https://doi.org/10.1039/D0NJ05557C.
[47] K.N. Rao, A. Sridhar, A.F. Lee, S.J. Tavener, N.A. Young, K. Wilson, Zirconium phosphate supported tungsten oxide solid acid catalysts for the esterification of palmitic acid, Green. Chem. 8 (2006) 790–797, https://doi.org/10.1039/b606088a.
[48] R. Luo, X. Zhao, H. Gong, W. Qian, D. Li, M. Chen, K. Cui, J. Wang, Z. Hou, Effect of Tungsten Modification on Zirconium Phosphate-Supported Pt Catalyst for Selective Hydrogenolysis of Glycerol to 1-Propanol, Energy Fuels 34 (2020) 8707–8717, https://doi.org/10.1021/acs.energyfuels.0c00645.
[49] B. Wang, F. Liu, W. Guan, A. Wang, T. Zhang, Promoting the Effect of Au on the Selective Hydrogenolysis of Glycerol to 1,3-Propanediol over the $Pt/WO_x/Al_2O_3$ Catalyst, ACS Sustain. Chem. Eng. 9 (2021) 5705–5715, https://doi.org/10.1021/acssuschemeng.1c00880.